Journal of ELECTRONIC MATERIALS, Vol. 44, No. 9, 2015
DOI: 10.1007/s11664-015-3823-4

As-Received CdZnTe Substrate Contamination

J.D. BENSON,[1,6] L.O. BUBULAC,[1] M. JAIME-VASQUEZ,[1] C.M. LENNON,[1] P.J. SMITH,[1] R.N. JACOBS,[1] J.K. MARKUNAS,[1] L.A. ALMEIDA,[1] A. STOLTZ,[1] J.M. ARIAS,[1] P.S. WIJEWARNASURIYA,[2] J. PETERSON,[3] M. REDDY,[3] M.F. VILELA,[3] S.M. JOHNSON,[3] D.D. LOFGREEN,[3] A. YULIUS,[4] M. CARMODY,[4] R. HIRSCH,[4] J. FIALA,[5] and S. MOTAKEF[5]

1.—U. S. Army RDECOM, CERDEC Night Vision and Electronic Sensors Directorate, Fort Belvoir, USA. 2.—U. S. Army Research Laboratory, Adelphi, USA. 3.—Raytheon Vision Systems, Goleta, USA. 4.—Teledyne Imaging Sensors, Camarillo, USA. 5.—CapeSym, Inc., Natick, USA. 6.—e-mail: david.j.benson@us.army.mil

State-of-the-art as-received (112)B CdZnTe substrates were examined for surface impurity contamination, polishing damage, and tellurium precipitates/inclusions. A maximum surface impurity concentration of Al = 7.5×10^{14}, Si = 3.7×10^{13}, Cl = 3.12×10^{15}, S = 1.7×10^{14}, P = 7.1×10^{13}, Fe = 1.0×10^{13}, Br = 1.9×10^{12}, and Cu = 4×10^{12} atoms cm^{-2} was observed on an as-received 6 × 6 cm wafer. As-received CdZnTe substrates have scratches and residual polishing grit on the (112)B surface. Polishing scratches are 0.3 nm in depth and 0.1 μm wide. The polishing grit density was observed to vary from wafer-to-wafer from $\sim 5 \times 10^6$ to 2×10^8 cm^{-2}. Te precipitate/inclusion size and density was determined by near-infrared automated microscopy. A Te precipitate/inclusion diameter histogram was obtained for the near-surface (top $\sim$140 μm) of a 6 × 6 cm substrate. The average areal Te precipitate/inclusion density was observed to be fairly uniform. However, there was a large density of Te precipitates/inclusions with a diameter significantly greater than the mean. Te precipitate/inclusion density > 10 μm diameter = 2.8×10^3 cm^{-3}. The large Te precipitates/inclusions are laterally non-uniformly distributed across the wafer.

Key words: CdZnTe substrate, molecular beam epitaxy, Te precipitate/inclusion, polishing damage, impurity contamination

INTRODUCTION

The highest sensitivity, lowest dark current HgCdTe infrared focal plane arrays (IRFPAs) are currently produced on CdZnTe substrates. A yield-limiting factor in MBE HgCdTe/CdZnTe detector fabrication is the presence of macro-defects[1] and wafer-to-wafer variability of focal plane array (FPA) yield. In previous work, two categories of HgCdTe epilayer macro-defects were associated with defects originating from the (112)B CdZnTe substrate surface.[2] Cross-sectional transmission electron microscopy (TEM) analysis traced micro-void defects to pits on the surface of the (112)B CdZnTe substrate.[3] Additional cross-sectional TEM analysis traced morphological defects to raised protrusions on the surface of the (112)B CdZnTe substrate.[2] In both TEM analyses, the defective area was confined to a small region surrounding the CdZnTe pit/protrusion and the HgCdTe epilayer micro-void/morphological defect.

In the current state-of-the-art HgCdTe detector, there is no buffer layer between the HgCdTe epilayer and the CdZnTe substrate. This makes the starting CdZnTe as-received surface and substrate preparation extremely critical for high-performance detector fabrication. The objective of this research is to analyze the initial 'out of the box' wafers for surface contamination, polishing damage, and Te precipitate/inclusion size/density in the near-surface region. Our working assumption is that lateral

(Received January 16, 2015; accepted April 30, 2015; published online June 5, 2015)

variations across a CdZnTe wafer and variability from CdZnTe wafer-to-wafer of impurity contamination, polishing damage, and Te precipitate/inclusion size/density are responsible for HgCdTe/CdZnTe macro-defects and FPA yield variability. The understanding of the impurity contamination, polishing damage, and Te precipitate/inclusion size and density is the first step toward developing more robust MBE CdZnTe preparation procedures capable of minimizing within-wafer and wafer-to-wafer variability.

EXPERIMENTAL

Nominal (112)B state-of-the-art CdZnTe substrates were analyzed in this work.[4] Examples of 1×1, 2×3, 4×4, and 6×6 cm (112)B CdZnTe wafers were analyzed. Nomarski phase contrast microscopy was used to locate morphological defects on the substrate surface.[5] Atomic force microscopy (AFM) and scanning profilometry were used to characterize surface topography and morphological defects in CdZnTe substrates. The AFM procedures have been described previously.[5] Scanning electron microscopy (SEM) and energy dispersive x-ray spectroscopy (EDS) were used to determine the composition of residual polishing grit found on the (112)B CdZnTe surface.

Near-infrared (near-IR) transmission microscopy was utilized to observe Te precipitate/inclusion size and density as well as to correlate with surface defects. The near-IR procedures have been described previously.[5] Additionally, an automated near-IR microscopy system was utilized to perform large wafer (6×6 cm) Te precipitate/inclusion analysis. This system has an automated routine for detecting, counting, and sizing the Te precipitates/inclusions.

Total reflection x-ray fluorescence (TXRF) measurements provided by Evans Analytical Group (EAG)[6] were used to analyze impurities on the surface of a 6×6 cm CdZnTe wafer. TXRF measurements were made using a TREX 630T TXRF instrument. The elements Al, Si, P, S, Cl, Cr, Mn, Fe, Ni, Cu, Zn, Ga, Ge, As, Br, Sr, Y, Ta, W, Pt, Au, Hg, Pb, and Bi could be measured using the Mo or W anode configuration to a detection limit of $\sim 1 \times 10^{10}$ atoms/cm^2. The analysis spot size was a ~10-mm-diameter circle. The analysis depth measured was ~2–3 nm on the CdZnTe (112)B surface. The concentration of impurities was calculated as a uniform contamination layer on the surface in atoms cm^{-2} over the area sampled. Quantification was performed using a Ni-plated Si reference wafer. The reference analysis conditions were corrected for differences between the x-ray optical properties of Si and CdZnTe surfaces. Because the area of the spot analysis is large, particle- and macro-contamination within the analysis spot can overestimate the reported surface density measurements.

A Φ 5800 MultiTechnique System high-vacuum analysis chamber containing XPS/Auger capabilities was also used for characterizing impurities on the wafer surface. The CdZnTe samples were mounted onto a stainless steel plate, secured with conductive clips, and inserted into the system. XPS data were acquired at a base pressure of 5×10^{-10} torr with monochromatic Al $K\alpha_{(1,2)}$ x-rays having an energy of 1486.6 eV, a pass energy of 2.95 eV, and a takeoff angle of 25°. This shallow angle was selected in order to examine the near-surface region, approximately 10 Å thick. All binding energies were corrected for charge shifting by referencing to the adventitious C1 s line at 284.6 eV. For the composition calculations, data obtained from an MgKα radiation source (1253.6 eV) were used. A standard calculation procedure was followed in which Shirley background subtraction and a 5-point smoothing was applied, then the line areas were divided by the respective sensitivity factors and normalized to total 100%.

RESULTS

Impurity Analysis

A 6×6 cm state-of-the-art as-received from the vendor (112)B CdZnTe wafer was analyzed using TXRF. A square-shaped analysis grid of 25 locations was measured as shown in Fig. 1a. The results from the impurity analysis are shown in Table I. The elements Cr, Mn, Ni, Ga, Ge, As, Sr, Y, Ta, W, Pt, Au, Hg, Pb, and Bi all had concentrations $\leq 1 \times 10^{12}$ atoms cm^{-2} on the as-received CdZnTe surface and are not shown in the table. Table I includes the maximum value, mean, standard deviation, coefficient of variation, and skew for each impurity element. Maximum impurity concentrations of Al = 7.5×10^{14}, Si = 3.7×10^{13}, Cl = 3.12×10^{15}, S = 1.7×10^{14}, P = 7.1×10^{13}, Fe = 1.0×10^{13}, Br = 1.9×10^{12}, and Cu = 4×10^{12} atoms cm^{-2} were found. In order to observe correlations in impurity contamination, the Pearson correlation coefficient (with values between +1 and −1, where 1 is total positive correlation, 0 is no correlation, and −1 is total negative correlation) was determined for each impurity element to all other elements. The results are shown in Table II. Because most of the impurity contamination does not vary widely across the sample, and many elements are near their detection limit, scatterplots for all Pearson correlation coefficients were produced to determine the linear least squares fit for the data. If $R^2 > 0.70$, then the impurity contamination between the two elements is said to be correlated. Figure 1b–d graphically represents the lateral impurity correlation profiles found using this procedure. In each of the figure parts, the area of the ball indicates the relative amount for each element. On each map, a representative 1 monolayer (ML -1.17×10^{15} atoms cm^{-2}) coverage ball is shown in the lower left corner (at position −25, −25 mm) for reference. As can be observed from Fig. 1b, there is a strong correlation of the lateral impurity concentration of Cu and Fe.

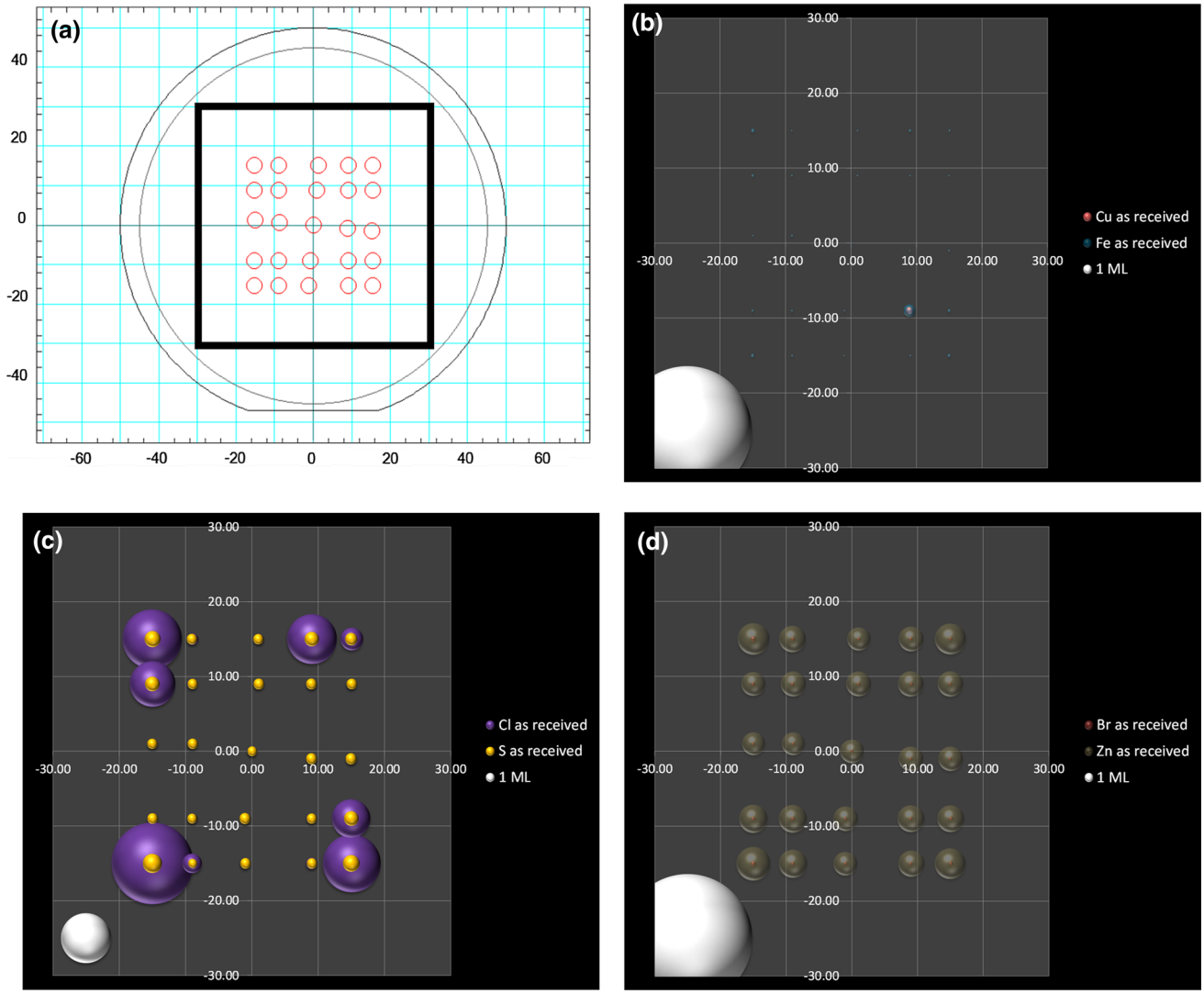

Fig. 1. TXRF measurements of a 6 × 6 cm state-of-the-art as-received from the vendor (112)B CdZnTe wafer. (a) Graphic representation of the square-shaped analysis grid of the 25 locations measured. (b–d) Graphical representation the lateral impurity correlation profiles. On each map, a representative 1 monolayer coverage ball is shown at position −25, −25 mm for reference. (b) Pearson correlation coefficient = 0.99 and R^2 = 0.99 for Cu and Fe. (c) Pearson correlation coefficient = 0.97 and R^2 = 0.94 for Cl and S. (d) Pearson correlation coefficient = 0.85 and R^2 = 0.72 for Br and Zn.

In Fig. 1c, a strong correlation of the lateral impurity concentration of Cl and S is shown. In Fig. 1d, a moderate correlation of the lateral impurity concentration of Br and Zn is shown.

XPS impurity analysis was performed on an as-received 2 × 3 cm (112)B CdZnTe substrate. Seven locations on the 2 × 3 cm CdZnTe wafer were analyzed as shown in Fig. 2. XPS is sensitive to most of the elements in the periodic table. Table III shows the results of this analysis for impurity elements found above the XPS detection limit. Table III also includes the maximum value, mean, standard deviation, coefficient of variation, and skew for each impurity element. As was observed in the TXRF analysis, high concentrations of Cl, Si, and S were detected on the (112)B CdZnTe surface. In addition, XPS detected F, O, and C. Maximum impurity concentrations of Si = 8.2×10^{13}, Cl = 2.0×10^{13}, S = 4.2×10^{13}, F = 5.9×10^{12}, O = 3.5×10^{14}, and C = 4.6×10^{14} atoms cm^{-2} were found. As was done previously, the Pearson correlation coefficient was determined for each impurity element to all other detected elements. The results are shown in Table IV. Again, because most of the impurity contamination does not vary widely across the sample, scatterplots for all Pearson correlation coefficients were produced to determine the linear least squares fit for data. If $R^2 > 0.70$, then the impurity contamination between the two elements is said to be correlated. For the XPS data, none of the impurity elements were found to be correlated using these criteria.

Polishing Analysis

As-received CdZnTe substrates were characterized for surface topography by AFM. Figure 3 shows

Table I. Results from the TXRF analysis at 25 locations on a 6 × 6 cm state-of-the-art as-received from the vendor (112)B CdZnTe wafer

X (mm)	*Y* (mm)	Al as received (at/cm^2)	Si as received (at/cm^2)	P as received (at/cm^2)	S as received (at/cm^2)	Cl as received (at/cm^2)	Fe as received (at/cm^2)	Cu as received (at/cm^2)	Br as received (at/cm^2)	Zn as received (at/cm^2)	Grit density (particles/cm^2)
−9.00	9.00	3.20E+14	1.30E+13	3.70E+13	4.70E+13	4.00E+13	2.7E+11	6.00E+10	8E+11	4.4E+13	1.40E+08
1.00	9.00	2.20E+14	9.00E+12	4.60E+13	5.30E+13	4.40E+13	2E+11	6.00E+10	7.7E+11	4.3E+13	1.60E+08
9.00	9.00	3.00E+14	8.00E+12	3.90E+13	5.40E+13	4.70E+13	2.1E+11	5.00E+10	7E+11	4.5E+13	1.30E+08
−9.00	1.00	2.30E+14	8.00E+12	3.00E+13	4.90E+13	4.50E+13	3E+11	6.00E+10	7.2E+11	3.7E+13	1.20E+08
0.00	0.00	2.10E+14	9.00E+12	2.70E+13	4.30E+13	3.90E+13	1.6E+11	5.00E+10	6.3E+11	3.9E+13	2.85E+08
9.00	−1.00	2.10E+14	9.00E+12	1.90E+13	5.50E+13	4.10E+13	1.5E+11	6.00E+10	8E+11	4.2E+13	1.00E+08
−9.00	−9.00	3.00E+14	9.00E+12	3.60E+13	4.40E+13	4.50E+13	2.4E+11	6.00E+10	1E+12	5.4E+13	5.60E+07
−1.00	−9.00	2.10E+14	9.00E+12	4.00E+13	5.60E+13	4.60E+13	1.7E+11	6.00E+10	7.4E+11	4.2E+13	1.80E+08
9.00	−9.00	7.50E+14	9.00E+12	3.00E+13	4.70E+13	4.10E+13	1.02E+13	4.00E+12	8E+11	5E+13	1.80E+08
−15.00	15.00	6.00E+14	2.00E+13	7.10E+13	1.19E+14	1.65E+15	1E+12	8.00E+10	1.9E+12	7E+13	1.20E+08
15.00	−15.00	5.90E+14	3.20E+13	6.50E+13	1.28E+14	1.56E+15	6.7E+11	8.00E+10	1.15E+12	6.6E+13	2.80E+08
−15.00	−15.00	7.00E+14	3.70E+13	5.80E+13	1.70E+14	3.12E+15	8.2E+11	8.00E+10	1.8E+12	8E+13	6.40E+07
15.00	15.00	5.70E+14	2.20E+1 3	6.50E+13	7.00E+13	2.39E+14	3.4E+11	8.00E+10	9E+11	6.7E+13	1.50E+08
15.00	9.00	3.30E+14	1.50E+13	3.40E+13	5.20E+13	4.20E+13	2.1E+11	5.00E+10	7E+11	4.5E+13	1.00E+08
15.00	−1.00	1.70E+14	1.00E+13	5.00E+13	5.60E+13	4.70E+13	2.4E+11	6.00E+10	7E+11	4.2E+13	1.70E+08
−15.00	1.00	1.90E+14	1.00E+13	3.60E+13	4.80E+13	3.80E+13	2E+11	5.0GE+10	6.3E+11	3.7E+13	1.20E+08
−1.00	−15.00	2.30E+14	1.80E+13	3.90E+13	5.10E+13	4.40E+13	1.4E+11	6.00E+10	8.3E+11	3.9E+13	1.40E+08
1.00	15.00	2.20E+14	2.10E+13	3.20E+13	4.80E+13	4.60E+13	2.3E+11	5.00E+10	7.2E+11	3.8E+13	1.20E+08
9.00	15.00	4.40E+14	2.20E+13	4.80E+13	9.70E+13	1.16E+15	5.2E+11	7.00E+10	9E+11	4.3E+13	1.70E+08
9.00	−15.00	3.40E+14	1.10E+13	3.10E+13	4.90E+13	5.70E+13	2.4E+11	5.00E+10	8.7E+11	4.8E+13	1.90E+08
−9.00	−15.00	3.70E+14	2.00E+13	4.10E+13	3.80E+13	1.75E+14	3.2E+11	6.00E+10	1E+12	5.6E+13	4.00E+07
−15.00	−9.00	3.90E+14	1.70E+13	4.50E+13	5.10E+13	4.50E+13	3.8E+11	6.00E+10	1.1E+12	5.6E+13	8.00E+07
−15.00	9.00	4.80E+14	1.20E+13	4.00E+13	9.80E+13	9.72E+14	4.9E+11	7.00E+10	9E+11	4E+13	1.60E+08
15.00	−9.00	4.50E+14	2.70E+13	5.40E+13	9.90E+13	6.88E+14	6.2E+11	7.00E+10	1.1E+12	5E+13	1.60E+08
−9.00	15.00	3.60E+14	1.60E+13	3.30E+13	5.00E+13	5.90E+13	1.8E+11	5.00E+10	1E+12	4.9E+13	1.10E+08
Maximum		7.50E+14	3.70E+13	7.10E+13	1.70E+14	3.12E+15	1.02E+13	4.00E+12	1.90E+12	8.00E+13	2.85E+08
Mean		3.67E+14	1.57E+13	4.18E+13	6.69E+13	4.13E+14	7.40E+11	2.19E+11	9.26E+11	4.89E+13	1.41E+08
Standard deviation		1.67E+14	7.89E+12	1.28E+13	3.28E+13	7.49E+14	1.98E+12	7.88E+11	3.15E+11	1.14E+13	5.83E+07
Coefficient of variation		0.45	0.50	0.31	0.49	1.82	2.68	3.59	0.34	0.23	0.41
Skew		088	1.19	0.73	1.85	2.46	4.90	5.00	2.17	1.31	0.79

Table II. Results of the Pearson correlation coefficient analysis of the TXRF data shown in Table I

	Al to Si	Al to P	Al to S	Al to Cl	Al to Fe	Al to Cu	Al to Br	Al to Zn	Al to Grit
pearson correlation coef	0.60	0.56	0.67	0.67	0.56	0.49	0.67	0.77	0.03
		Si to P	Si to S	Si to Cl	Si to Fe	Si to Cu	Si to Br	Si to Zn	Si to Grit
	pearson correlation coef	0.67	0.78	0.77	-0.10	-0.17	0.67	0.70	-0.04
			P to S	P to Cl	P to Fe	P to Cu	P to Br	P to Zn	P to Grit
		pearson correlation coef	0.71	0.64	-0.10	-0.18	0.67	0.73	0.09
				S to Cl	S to Fe	S to Cu	S to Br	S to Zn	S to Grit
			pearson correlation coef	0.97	-0.03	-0.12	0.78	0.68	0.09
					Cl to Fe	Cl to Cu	Cl to Br	Cl to Zn	Cl to Grit
				pearson correlation coef	0.00	-0.09	0.82	0.71	-0.01
						Fe to Cu	Fe to Br	Fe to Zn	Fe to Grit
					pearson correlation coef	0.99	0.02	0.10	0.14
							Cu to Br	Cu to Zn	Cu to Grit
						pearson correlation coef	-0.07	0.03	0.14
								Br to Zn	Br to Grit
							pearson correlation coef	0.85	-0.26
									Zn to Grit
								pearson correlation coef	-0.19

Pearson correlation coefficient

100-96	95-91	90-86	85-81	80-76	75-71	70-60

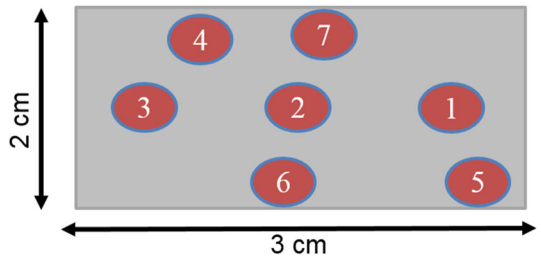

Fig. 2. Graphic representation of the seven locations measured by XPS analysis of a 2 × 3 cm state-of-the-art as-received from the vendor (112)B CdZnTe wafer.

AFM images of the as-received (112)B CdZnTe surface from 1 × 1, 4 × 4, and 6 × 6 cm wafers. The root mean squared (RMS) roughness of all the wafers is ~0.4 nm (determined at both the center and edge). CdZnTe surfaces are vulnerable to polishing damage in the form of surface scratches.[7] As can be observed from all three images, the final polishing step leaves scratches and residual polishing grit on the (112)B surface. The 'deep' polishing scratches are 0.3 nm in depth and 0.1 μm wide. Polishing grit particle length varied from 100 nm to 1 μm. The height of the polishing grit was measured to be between 10 nm and 300 nm above the (112)B surface. The polishing grit density was observed to vary from wafer-to-wafer from $\sim 5 \times 10^6$ to 2×10^8 cm^{-2}. In Fig. 3d, a map of the residual polishing grit density for a 6 × 6 cm wafer is shown. There is a factor of 7 variation of residual polishing grit density across the 6 × 6 cm wafer.

In Fig. 4, a high resolution SEM image of 1 'large' and 1 small piece of polishing grit residue are shown along with the corresponding EDS profile of the 'large' piece. The large piece of polishing grit is

Table III. Results from the XPS analysis at 7 locations on a 2 × 3 cm state-of-the-art as-received from the vendor (112)B CdZnTe wafer

Area	*X* (cm)	*Y* (cm)	Cl as received (at. cm^{-2})	Si as received (at. cm^{-2})	S as received (at cm^{-2})	F as received * (at. cm^{-2})	Oas received (at. cm^{-2})	Cas received (at. cm^{-2})	Te oxide thickness (nm)
1	1.2	0	7.00E+12	7.00E+13	4.20E+13	1.00E+12	3.50E+14	3.70E+14	0.28
2	0	0	1.30E+13	5.90E+13	3.00E+13	1.00E+12	2.80E+14	3.70E+14	0.33
3	−1.2	0	1.60E+13	7.00E+13	3.90E+13	1.00E+12	2.80E+14	4.20E+14	0.34
4	−1	0.8	2.00E+13	8.20E+13	3.60E+13	5.90E+12	3.20E+14	4.40E+14	0.28
5	1.3	−0.8	1.80E+13	8.20E+13	3.50E+13	1.00E+12	3.40E+14	4.10E+14	0.27
6	−0.1	−0.8	1.90E+13	7.00E+13	4.10E+13	1.00E+12	3.30E+14	4.30E+14	0.26
7	0.1	0.8	1.80E+13	8.20E+13	3.00E+13	1.00E+12	2.90E+14	4.60E+14	0.23
Maximum			2.00E+13	8.20E+13	4.20E+13	5.90E+12	3.50E+14	4.60E+14	0.34
Mean			1.59E+13	7.36E+13	3.61E+13	1.70E+12	3.13E+14	4.14E+14	0.28
Standard deviation			4.53E+12	8.79E+12	4.88E+12	1.85E+12	2.93E+13	3.41E+13	0.04
Coefficient of variation			0.29	0.12	0.14	1.09	0.09	0.08	0.14
Skew			−1.50	−0.49	−0.25	2.65	−0.06	−0.34	0.37

Table IV. Results of the Pearson correlation coefficient analysis of the XPS data shown in Table III

	Cl to Si	Cl to S	Cl to F	Cl to O	Cl to C	Cl to Te Oxide
pearson correlation coef	0.56	-0.26	0.40	-0.19	0.83	-0.31
		Si to S	Si to F	Si to O	Si to C	Si to Te Oxide
	pearson correlation coef	-0.08	0.42	0.32	0.72	-0.68
			S to F	S to O	S to C	S to Te Oxide
		pearson correlation coef	-0.01	0.60	-0.17	0.08
				F to O	F to C	F to Te Oxide
			pearson correlation coef	0.11	0.33	-0.05
					O to C	O to Te Oxide
				pearson correlation coef	-0.18	-0.45
						C to Te Oxide
					pearson correlation coef	-0.56

Pearson correlation coefficient

100-96	95-91	90-86	85-81	80-76	75-71	70-60

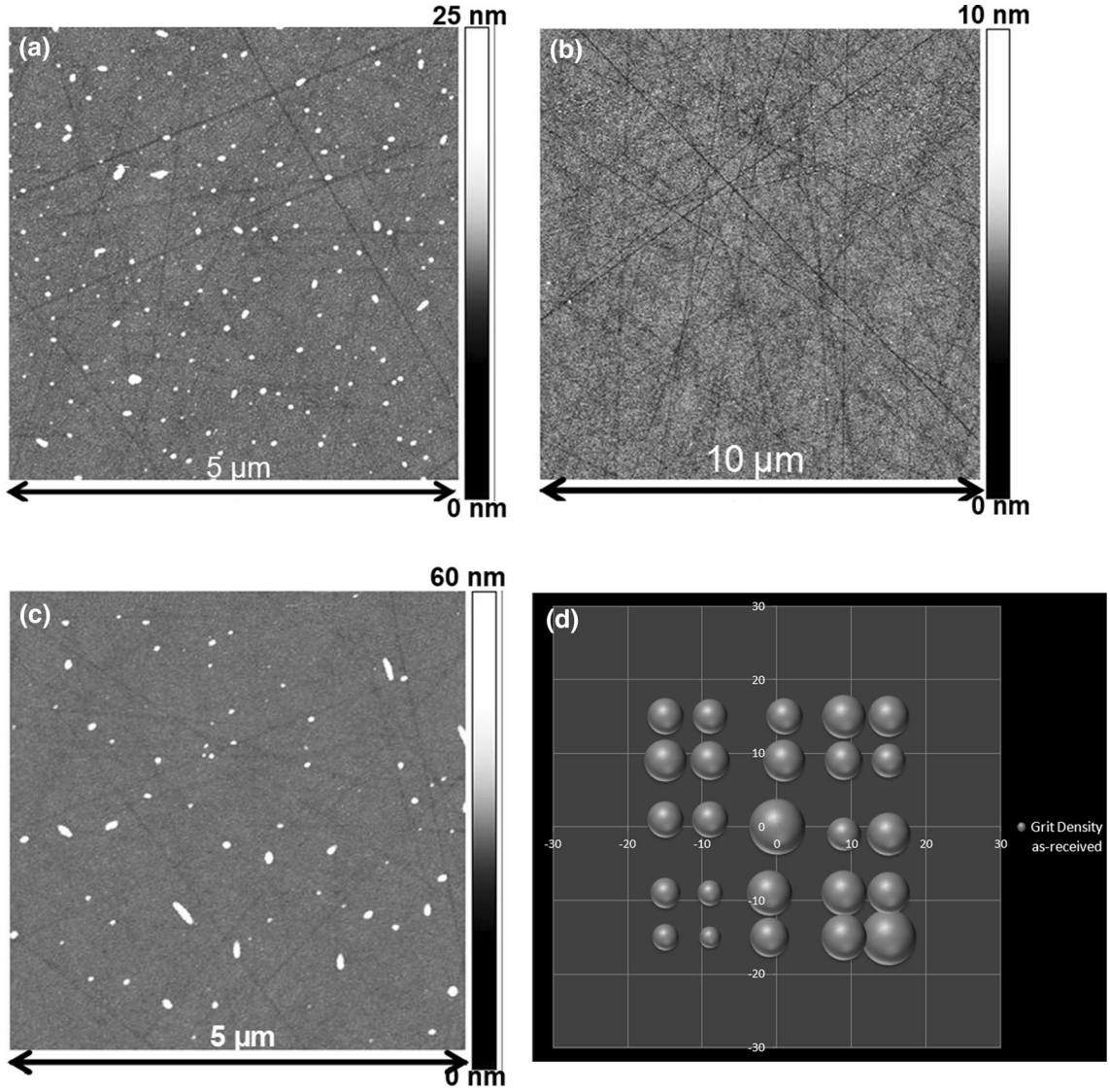

Fig. 3. AFM measurements of as-received (112)B CdZnTe surfaces. (a) Image of the center of a 1 × 1 cm wafer showing polishing scratches and residual polishing grit. (b) The center of 4 × 4 cm wafer shows polishing scratches and a relatively small amount of residual polishing grit. (c) Image of the center of 6 × 6 cm wafer showing polishing scratches and residual polishing grit. (d) A graphical representation of the residual polishing grit density for 25 locations on a 6 cm × 6 cm wafer.

composed of SiO_2. The 'large' polishing grit particle is ~0.35 μm in length. The 'small' polishing grit particle is ~0.05 μm in diameter. The 'large' piece of polishing grit appears to be an agglomeration of smaller pieces of grit. Polishing grit appears to be electrostatically bound to the top surface layer of the CdZnTe as shown in the SEM image in Fig. 4. Dislodging residual 'large' polishing grit pieces was attempted using the AFM tip as a manipulator. This proved unsuccessful.

Te Precipitates/Inclusions in the Near-Surface Region

It is well known that CdZnTe substrates have Te precipitates/inclusions.[8–11] Typical Te precipitate/inclusion density in state-of-the-art CdZnTe is $\sim 2 \times 10^6$ cm^{-3}. The typical Te precipitate/inclusion diameter in state-of-the-art CdZnTe is ~2–3 μm (high resolution images of Te precipitates/inclusions are shown in Ref.5). Using an automated near-IR microscope and Te precipitate/inclusion counting routine, the Te precipitates/inclusions in a 6 × 6 cm wafer were mapped in the near-surface region (top ~140 μm). The Te precipitate/inclusion map is shown in Fig. 5a. The average areal Te precipitate/inclusion density across the 6 × 6 cm wafer is relatively laterally uniform. A histogram of the Te precipitate/inclusion diameter is shown in Fig. 5b. The mean Te precipitate/inclusion diameter is 1.5–2.5 μm. This result is typical of state-of-the-art CdZnTe wafers. There are a large number of Te

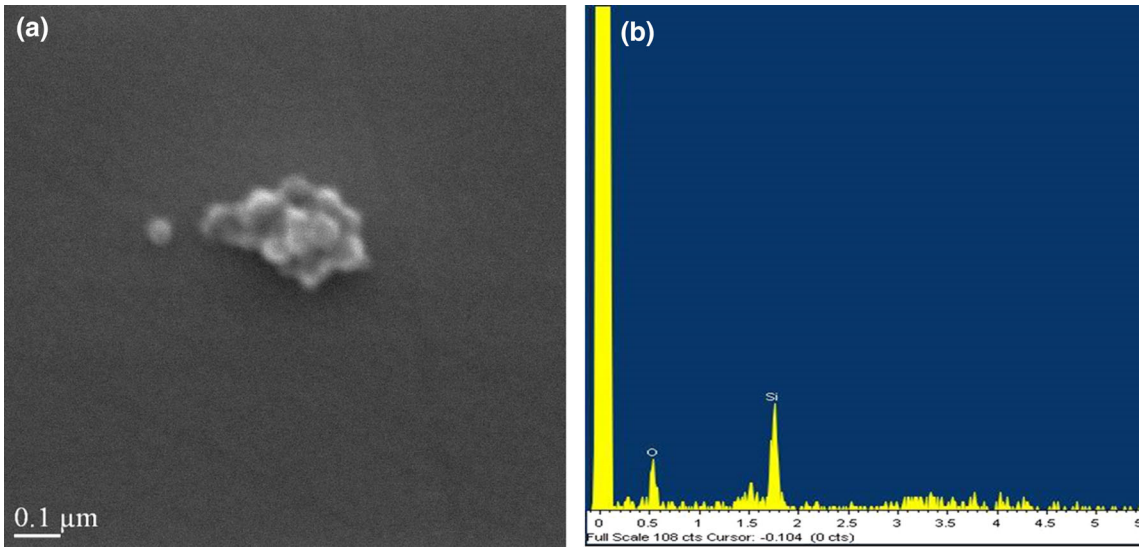

Fig. 4. (a) High-resolution SEM image of 1 'large' and 1 small piece of polishing grit residue. (b) The corresponding EDS profile of the 'large' piece.

precipitates/inclusions with greater diameter than the mean. Te precipitate/inclusion density with >10 μm diameter = 2.8×10^3 cm^{-3}. The large Te precipitates/inclusions are laterally non-uniformly distributed across the 6×6 cm wafer as shown in Fig. 5c.

DISCUSSION

The analysis of the as-received wafers clearly demonstrates that they are not 'epi-ready out of the box'. In both the TXRF and XPS analyses, surface impurity concentrations are well above the acceptable level for standard semiconductor processing.[12] Additionally, the wide lateral variation (coefficient of variation >1 and skew >2) in surface contamination of Cl, Fe, Cu, and F observed in Tables I and III makes uniform HgCdTe processing problematic. The EDS spectra shown in Fig. 4 demonstrates that some of the Si contamination found in both the TXRF and XPS analysis is coming from residual SiO_2 polishing grit. The authors speculate that the Al contamination is coming from residual Al_2O_3 polishing grit (future EDS experiments are required to confirm this hypothesis). P, Fe and Cu are potential contaminates in polishing grit slurry. Fe could also be coming from dicing the CdZnTe wafer. P and Fe may additionally be cross-contamination from other semiconductor polishing (such as InP substrates). The authors speculate that Cl contamination is due to NaClO which is used as a standard polishing slurry cleaner.

Te precipitates/inclusions are known to getter impurities in CdZnTe substrates and prevent impurities from reaching the deposited HgCdTe epitaxial thin films.[13–18] Impurities in CdZnTe substrates can diffuse into HgCdTe deposited on these substrates by liquid phase epitaxy (LPE), metal–organic chemical vapor deposition (MOCVD), or MBE.[14] Impurities diffusing from the CdZnTe substrate can affect carrier concentration, mobility, and minority carrier lifetime in the HgCdTe epilayer.[16] The density and size of Te precipitates/inclusions in CdZnTe has further been demonstrated to impact the electrical transport properties of deposited HgCdTe.[14] It has also been demonstrated that Te precipitate/inclusion-related defects near the growth surface of the (112)B CdZnTe substrate affect MBE-deposited HgCdTe epilayers.[1–3,5] Since Te precipitate/inclusion-related defects, particularly small pits and raised protrusions in (112)B CdZnTe substrates, have been previously linked to micro-void and morphological defects in the HgCdTe epilayer, the large number of >10 μm diameter Te precipitates/inclusions is very concerning. After MBE HgCdTe deposition, these large Te precipitates/inclusions could lead to localized micro-void and morphological defects as well as localized impurity centers.

The CdZnTe wafers surface impurities and damage layers dictate that an MBE preparation etch is required. The ultimate goal for the MBE preparation etch technique is to provide a clean, stoichiometric, atomically smooth, and well-ordered surface to minimize growth defects. The contamination levels and surface damage dictate the requirements that the preparation etch needs to achieve to produce a wafer ready for MBE HgCdTe epitaxial deposition. Investigating the current MBE preparation etch for its ability to reduce the contamination and damage left on the as-received wafers will be the next step in this on-going CdZnTe substrate investigation.

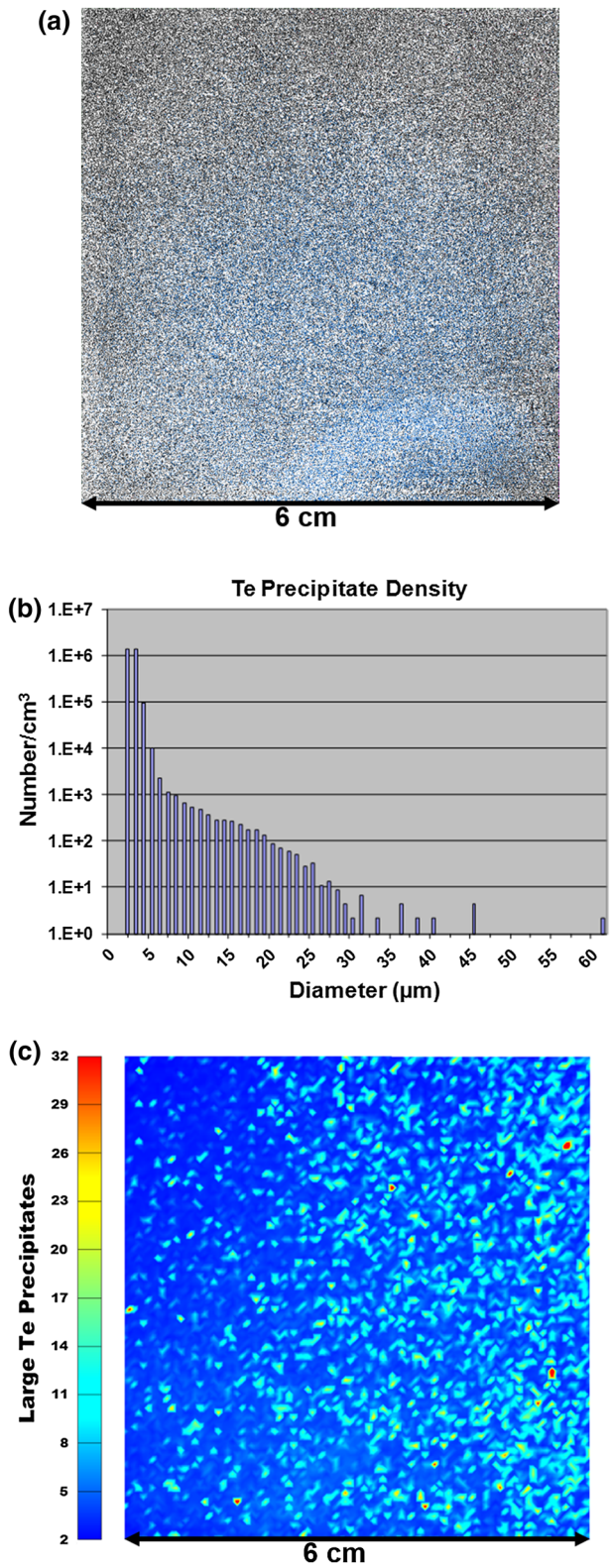

Fig. 5. Top ~140 μm of a 6 × 6 cm wafer were mapped with an automated near-IR microscope. (a) Te precipitate/inclusion map. (b) Histogram of the Te precipitate/inclusion diameter. (c) The locations of large Te precipitates/inclusions are highlighted in red (Color figure online).

CONCLUSIONS

As-received CdZnTe wafers were characterized for surface topography and polishing damage, impurity contamination, and Te precipitate/inclusion density and size. A 6 × 6 cm state-of-the-art as-received from the vendor (112)B CdZnTe wafer was analyzed using TXRF. Maximum surface impurity concentrations of Al = 7.5×10^{14}, Si = 3.7×10^{13}, Cl = 3.12×10^{15}, S = 1.7×10^{14}, P = 7.1×10^{13}, Fe = 1.0×10^{13}, Br = 1.9×10^{12}, and Cu = 4×10^{12} atoms cm^{-2} were observed. The elements Cr, Mn, Ni, Ga, Ge, As, Sr, Y, Ta, W, Pt, Au, Hg, Pb, and Bi all had concentrations ≤1×10^{12} atoms cm^{-2} on the as-received CdZnTe surface. Impurity analysis by XPS was performed on an as-received 2 × 3 cm CdZnTe substrate. XPS analysis found maximum impurity concentrations of Si = 8.2×10^{13}, Cl = 2.0×10^{13}, S = 4.2×10^{13}, F = 5.9×10^{12}, O = 3.5×10^{14}, and C = 4.6×10^{14} atoms cm^{-2}.

The as-received wafers were characterized for surface topography and polishing damage. The final polishing step leaves scratches and residual polishing grit. Polishing scratches were 0.3 nm in depth and 0.1 μm wide. The polishing grit density was observed to vary from wafer-to-wafer from ~5×10^6 to 3×10^8 cm^{-2}. There was a factor of 7 variation of residual polishing grit density across a 6 × 6 cm wafer. An EDS profile of a 'large' piece of polishing grit showed that it is composed of SiO_2. The 'large' piece of polishing grit appeared to be an agglomeration of smaller pieces of polishing grit. Polishing grit appeared to be electrostatically held on the top surface of the CdZnTe.

Te precipitates/inclusions in a 6 × 6 cm wafer were mapped in the near-surface region (top ~140 μm). The mean Te precipitate/inclusion diameter was 1.5–2.5 μm. Tellurium precipitate/inclusion density was observed to be fairly uniform across a 6 × 6 cm wafer. There were a large number of Te precipitates/inclusions with greater than the mean diameter. Te precipitate/inclusion density >10 μm diameter = 2.8×10^3 cm^{-3}. The large Te precipitates/inclusions were laterally non-uniformly distributed across a 6 × 6 cm wafer.

The as-received wafers were not epi-ready 'out of the box'. The wafers surface damage and impurity levels dictate that an MBE preparation etch is required. The ultimate goal for the MBE preparation etch technique is to provide a clean, stoichiometric, atomically smooth, and well-ordered surface to minimize growth defects.

REFERENCES

1. M. Reddy, J. Wilde, J.M. Peterson, D.D. Lofgreen, and S.M. Johnson, *J. Electron. Mater.* 41, 2957 (2013).
2. M. Reddy, W.A. Radford, D.D. Lofgreen, K.R. Olsson, J.M. Peterson, and S.M. Johnson, *J. Electron. Mater.* 43, 2991 (2014).

3. M. Reddy, D.D. Lofgreen, K.A. Jones, J.M. Peterson, W.A. Radford, J.D. Benson, and S.M. Johnson, *J. Electron. Mater.* 42, 3114 (2013).
4. JX Nippon Mining & Metal Corporation (January 2015): www.nikkometals.com.
5. J.D. Benson, L.O. Bubulac, P.J. Smith, R.N. Jacobs, J.K. Markunas, M. Jaime-Vasquez, L.A. Almeida, A. Stoltz, P.S. Wijewarnasuriya, G. Brill, Y. Chen, J. Peterson, M. Reddy, M.F. Vilela, S.M. Johnson, D.D. Lofgreen, A. Yulius, G. Bostrup, M. Carmody, D. Lee, and S. Couture, *J. Electron. Mater.* 43, 3993 (2014).
6. Evans Analytical Group (January 2015): www.eag.com/mc/total-reflection-x-ray-fluorescence.html.
7. C.K. Egan, P. Dabrowski, Z. Klusek, and A.W. Brinkman, *J. Electron. Mater.* 38, 1528 (2009).
8. H.R. Vydyanath, J.A. Ellsworth, J.B. Parkinson, J.J. Kennedy, B. Dean, C.J. Johnson, G.T. Neugebaur, J. Sepich, and P.K. Liao, *J. Electron. Mater.* 22, 1073 (1993).
9. T.S. Lee, J.W. Park, Y.T. Jeoung, H.K. Kim, C.H. Chun, J.M. Kim, I.H. Park, J.M. Chang, S.U. Kim, and M.J. Park, *J. Electron. Mater.* 24, 1053 (1995).
10. S. Sen, C.S. Liang, R.R. Rhiger, J.E. Stannard, and H.F. Arlinghaus, *J. Electron. Mater.* 25, 1188 (1996).
11. A. Noda, H. Kurita, and R. Hirano, *Mercury Cadmium Telluride Growth, Properties and Applications*, ed. P. Capper and J. Garland (West Sussex: Wiley, 2011), pp. 21–49.
12. W. Kern, *Handbook of Silicon Wafer Cleaning Technology*, 2nd ed., ed. K.A. Reinhardt and W. Kern (William Andrew: Norwich, 2008), pp. 4–13.
13. J.P. Tower, S.P. Tobin, P.W. Norton, A.B. Bollong, A. Socha, J.H. Tregilgas, C.K. Ard, and H.F. Arlinghaus, *J. Electron. Mater.* 25, 1183 (1996).
14. R. Korenstein, R.J. Olson, D. Lee, P.K. Liao, and C.A. Castro, *J. Electron. Mater.* 24, 511 (1995).
15. H.F. Schaake, J.H. Tregilgas, M.A. Kinch, and B.E. Gnade, *J. Vac. Sci. Technol.* A3, 143 (1985).
16. T.H. Myers, K.A. Harris, R.W. Yanka, L.M. Mohnkern, R.J. Williams, and G.K. Dudoff, *J. Vac. Sci. Technol.* B10, 1438 (1992).
17. G. Yang, A.E. Bolotnikov, Y. Cui, G.S. Camarda, A. Hossain, and R.B. James, *J. Cryst. Growth* 311, 99 (2008).
18. E. Weiss, O. Klin, E. Benory, E. Kedar, and Y. Juravel, *J. Electron. Mater.* 30, 756 (2001).